Tectonophysics xxx (2016) xxx–xxx

Contents lists available at ScienceDirect

Tectonophysics

journal homepage: www.elsevier.com/locate/tecto

The magmatic system beneath the Tristan da Cunha Island: Insights from thermobarometry, melting models and geophysics

Anne Weit [a,b,*], Robert B. Trumbull [b], Jakob K. Keiding [b,c], Wolfram H. Geissler [d], Sally A. Gibson [e], Ilya V. Veksler [b]

[a] Department of Earth Sciences, Free University of Berlin, Germany
[b] GFZ German Research Centre for Geosciences, Potsdam, Germany
[c] Geological Survey of Norway, Trondheim, Norway
[d] Alfred-Wegener Institute, Bremerhaven, Germany
[e] Department of Earth Sciences, University of Cambridge, Cambridge, UK

ARTICLE INFO

Article history:
Received 29 February 2016
Received in revised form 16 July 2016
Accepted 10 August 2016
Available online xxxx

Keywords:
Geothermobarometry
Melt inclusions
REE inversion model
Tristan hotspot
Moho

ABSTRACT

This study provides new insights on the conditions of melt generation and of magma transport and storage beneath Tristan da Cunha Island in the South Atlantic. Situated at the seaward end of the Walvis Ridge-guyot hotspot track, this island is related to the evolving magmatic system of the Tristan plume. Much is known about the geochemical and isotopic composition of the alkaline lavas on Tristan, but the pressure–temperature conditions of the hotspot magmas are under-explored. This contribution reports new data from a suite of 10 samples collected during a geologic–geophysical expedition in 2012. The focus of this study is on the least-evolved, phenocryst-rich basanite lavas but we also included a sample of trachyandesite lava erupted in 1961. Mineral-melt equilibrium thermobarometry uses the composition of olivine, clinopyroxene and plagioclase phenocrysts. In addition to bulk-rock data we also analysed olivine-hosted melt inclusions for the P–T calculations. The results for olivine-melt and clinopyroxene-melt calculations suggest crystallization conditions of around 1200–1250 °C and 0.8–1.3 GPa for the least-evolved magmas (ankaramitic basanites). Combined with seismological evidence for a Moho depth of about 19 km, these results imply magma storage and partial crystallization of Tristan magmas in the uppermost mantle and at Moho level. The trachyandesite yielded values of about 1000 °C and 0.2–0.3 GPa (6 to 10 km depth), indicating further crystallization within the crust.

Constraints on the depth and degree of melting at the source of Tristan basanites were derived from REE inverse modelling using our new trace element data. The model predicts 5% melt generation from a melting column with its base at 80–100 km and a top at 60 km, which is consistent with the lithospheric thickness resulting from cooling models and seismological observations. The thermobarometry and melting models combined suggest a mantle potential temperature of about 1360 °C for the Tristan hotspot.

1. Introduction

The island of Tristan da Cunha in the South Atlantic belongs to a volcanic archipelago at the southwestward end of a seamount chain which, together with the Ridge, reflects a hotspot track that formed during the Cretaceous separation of South America from Africa (O'Connor and Duncan, 1990; O'Connor et al., 2012; Rohde et al., 2012). Many studies of magma genesis in the Paraná–Etendeka Large Igneous Province have taken Tristan da Cunha lavas to reflect the present-day composition of the Tristan mantle plume (e.g. Ewart et al., 1998, 2004; Harris et al., 1999; Hawkesworth et al., 1999; Thompson et al., 2001; Trumbull et al., 2003; Gibson et al., 2005; Rocha-Junior et al., 2012; Rocha-Junior et al., 2013). However, recent work has shown that the mantle source(s) and melting regime along the hotspot track have evolved over time since the early Cretaceous Tristan plume (Le Roex et al., 1990; Harris et al., 2000; Gibson et al., 2005; Hicks et al., 2012; Rohde et al., 2013; Hoernle et al., 2015). The picture emerging is one of a diminishing intensity of the plume with time, along with a change in the proportions of mantle components that are melting within it. Rohde et al. (2013) and Hoernle et al. (2015) demonstrated geochemical differences between the Tristan and Gough islands and their respective seamount chains that suggest a compositionally-zoned plume has persisted since separation of the Walvis Ridge from the Atlantic spreading center at about 80 Ma. Gibson et al. (2005) argued from geochemical–petrologic models that the potential temperature in the mantle source had decreased from around 1500 °C in the Etendeka Province to 1450 °C before hotspot-ridge separation at 80 Ma to around 1350 °C for the Tristan archipelago today.

* Corresponding author at: University Blaise-Pascal Clermont Ferrand, France.
E-mail address: a.weit@opgc.univ-bpclermont.fr (A. Weit).

http://dx.doi.org/10.1016/j.tecto.2016.08.010
0040-1951/

None of the previous studies addressed the question of magma temperatures and pressures recorded in the phenocryst assemblage of Tristan lavas and their implications for the geometry of the "plumbing system" under the hotspot island. That is the main goal of a new geochemical and petrologic study of Tristan da Cunha mafic lavas reported here, where we shed light on the conditions of magma crystallization based on analyses of olivine and clinopyroxene phenocrysts in Tristan da Cuhna lavas and, crucially, of the melt inclusions preserved in olivine. In their detailed geochemical study of Tristan lavas le Roex et al. (1990) established the main geochemical and isotopic features of Tristan magmas and proposed a conceptual model of magma genesis and evolution. Our new trace element analyses include the full REE spectrum and concentrations of other incompatible trace elements not previously determined, and we use those data for inversion modelling to better understand the melting regime in the mantle below the Tristan archipelago. Finally, we compare the petrological constraints on magma generation and storage depths with seismic S-wave velocity variations in the crust and uppermost mantle beneath the Tristan group islands based on new seismological studies (Geissler et al., 2016).

2. Geologic background and previous work

Tristan da Cunha is the largest of three neighboring islands comprising the Tristan da Cunha group, the others being Inaccessible and Nightingale (Fig. 1). With its highest point at 2060 m above sea level, the nearly conical volcano rises about 5.5 km above the seafloor. Tristan lavas are all younger than 0.5 Ma (Hicks et al., 2012) and the island is still volcanically active: the most recent eruption being in 1961, which

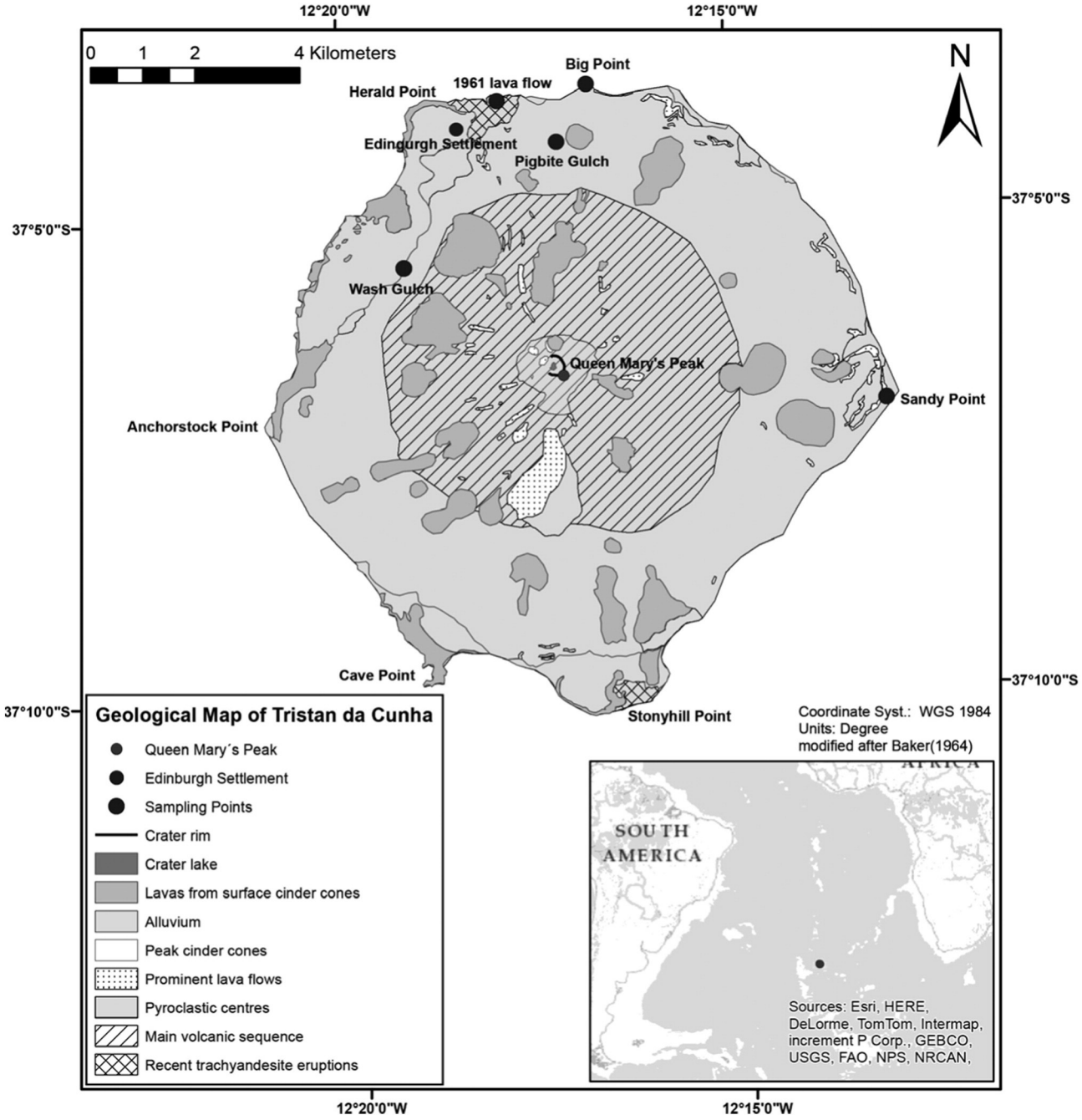

Fig. 1. Geologic map of Tristan da Cunha showing sample location points for this study. after Baker et al. (1962)

Please cite this article as: Weit, A., et al., The magmatic system beneath the Tristan da Cunha Island: Insights from thermobarometry, melting models and geophysics, Tectonophysics (2016), http://dx.doi.org/10.1016/j.tecto.2016.08.010

caused the island to be evacuated and motivated the volcanologic expedition of Baker et al. (1962). Tristan da Cunha is built of a series of lava flows, dykes and pyroclastic deposits. Apart from the central vent, there are over thirty secondary scoria cones and lava vents on all flanks of the volcano (Baker et al., 1962). The 1961 eruption emanated from one such vent at the base of the northern slope (Fig. 1). Submarine activity to the south(east) of the main volcano in 2004 was evidenced by seismic tremors and phonolitic pumice washed up on the shores of the island (Reagan et al., 2008; O'Mongain et al., 2007).

The petrography and chemical composition of Tristan volcanic rocks were described by Baker et al. (1962), who established that basanite (trachybasalt in their terminology) is the dominant rock type (~80%), exposed on all parts of the island, followed by moderate amounts of phonotephrite (~15%) and minor occurrences of more evolved rocks (trachyandesite and phonolite) of which the 1961 eruption is one example. The main volcanic edifice (shield) of interlayered lava and pyroclastic flows has not been well dated but it must be older than 118 ka based on the ^{40}Ar–^{39}Ar study by Hicks et al. (2012), which determined 15 dates for parasitic post-shield volcanism on flanks and coastal plains throughout the island. They reported a spread of ages from 118 ± 4 ka to 3 ± 1 ka, and noted the systematic progression towards more evolved compositions with time but there is no apparent spatial pattern of the age variations.

The first detailed geochemical study of Tristan lavas, including trace elements and radiogenic isotope data, was by le Roex et al. (1990), who produced fractionation models that accounted for much of the compositional diversity in the rock series. Using those same samples, Harris et al. (2000) determined the oxygen isotope ratios of olivine, clinopyroxene and feldspar phenocrysts and concluded that some magmas were contaminated by older, hydrothermally-altered lavas which lowered their O-isotope ratios below the typical mantle value. Although both of these studies mentioned mineral compositions, ours is the first study to publish an extensive data set of mineral chemistry.

3. Samples and methods

The samples used in this study were collected in 2012 during a stop on the island by the research vessel RV Maria S. Merian, which also conducted geophysical experiments and detailed bathymetry surveys in the region around the Tristan and Gough islands. The emphasis of sampling was on olivine-rich akaramitic basanites and four localities of these were chosen based on previous work: Sandy Point in the east; Big Point, Pigbite (Plantation) Gulch and Wash Gulch in the north and north-west (Fig. 1). A lava flow of the 1961 eruption from a locality east from the settlement was also sampled for comparison. Table 1 lists the sample set with locations and ages from the $^{40}Ar/^{39}Ar$ study by Hicks et al. (2012) where our sample locations correspond to dated localities.

3.1. Bulk rock analyses

All rock analyses were performed at the GFZ Potsdam. Rock samples were freed of alteration rinds by hammer and chisel, then cleaned with water, dried and jaw-crushed. Aliquots of about 100 g of crushed rock were ground to <63 μm powder in an agate mill. The sieved, powdered samples were analysed by X-ray fluorescence spectroscopy on fused glass discs using a PANalytical AXIOS Advanced instrument with a Rh tube. Volatile components H_2O and CO_2 were analysed by infrared spectroscopy. Additional trace elements were determined on a subset of samples by inductively coupled plasma mass spectrometry, using a Sciex Elan Model 5000A instrument following methods described by Dulski (2001).

3.2. Electron microprobe analyses

Mineral compositions were determined in-situ on polished, carbon-coated thin sections using a JEOL JXA-8230 electron microprobe with wavelength-dispersive spectrometers. The electron microprobe analyses of melt inclusions in olivine crystals were performed on 25 cm diameter, polished epoxy mounts of olivine grains selected after homogenization runs (see below). The electron microprobe was operated at 15 kV accelerating voltage and a beam current of 15 nA, with a fully-focused (ca. 1 μm) beam for clinopyroxene and olivine. Plagioclase and melt inclusion glass were analysed using a defocused 5 μm beam and Na was measured first in the element sequence to minimize the effects of alkali loss. Replicate analyses of natural and synthetic standards indicate that the precision of major oxides (>0.2 wt.%) is ±9% (2σ) or better. Correction of the measured intensities used the PAP method. In total, approximately 900 point analyses for olivine, plagioclase, clinopyroxene and oxide phases were determined. The full data set is given in the Supplementary data. Average compositions of olivine, clinopyroxene and plagioclase from the samples used for geothermobarometry are reported in Section 4.5 (Table 3).

3.3. Melt inclusions

Olivine-hosted melt inclusions were initially searched for in standard thin sections, and from selected samples (basanite TDC-12-2 and TDC-12-8). Olivine phenocrysts with inclusions were subsequently hand-picked from grain separates for study. All melt inclusions are partly crystalline and required homogenisation before analysis. This was done in a vertical gas-mixing tube furnace held at 1200 °C, which corresponds to the estimated liquidus temperature at 1 atm predicted by phase equilibrium calculations using host rock composition and confirmed by preliminary trial runs. Redox conditions close to the quartz–fayalite–magnetite buffer were maintained by the CO_2–Ar–H_2 gas mixture and controlled by a solid zirconia electrolyte cell. Olivine crystals with melt inclusions were loaded into a platinum crucible and heated for approximately 10 min, then removed from the furnace and quenched on a cold metal plate. After cooling the olivine crystals were cast in epoxy mounts, then ground and polished for microprobe analysis. Fig. 2 shows typical examples of unheated and homogenized melt inclusions. The darker rim of the olivine host crystal immediately surrounding the homogenized inclusion is probably due to incomplete quench-olivine crystallization on inclusion walls (see below and Danyushevsky et al., 2000).

4. Results

4.1. Petrography and mineral chemistry

The samples collected for this study are comprised of basanite to trachyandesite, whose bulk compositions cover most of the range established by Le Roex et al. (1990). The ankaramite samples (e.g., crystal-rich basanite with dominant clinopyroxene) contain up to 50% by volume of phenocrysts (clinopyroxene and olivine, minor plagioclase and Ti-magnetite). By definition, clinopyroxene is more abundant than olivine, but in some samples the volume fraction of olivine phenocrysts reaches 20–25%. The groundmass is composed of plagioclase laths, anhedral clinopyroxene grains and very fine-grained Fe–Ti oxides. Typical examples are illustrated in Fig. 3. The sample of lava from the 1961 eruption (TDC-12-1) is a fine-grained and weakly porphyritic trachyandesite. The phenocryst assemblage constitutes about 35 vol% of the rock and it is dominated by euhedral to subhedral plagioclase crystals up to 2 mm in length, with minor amounts of clinopyroxene (5–7 vol% of the rock) and lesser amphibole and Fe–Ti oxide grains. Olivine is absent. The fine-grained groundmass is composed of elongated tabular plagioclase microphenocrysts up to

Please cite this article as: Weit, A., et al., The magmatic system beneath the Tristan da Cunha Island: Insights from thermobarometry, melting models and geophysics, Tectonophysics (2016), http://dx.doi.org/10.1016/j.tecto.2016.08.010

Table 1
Whole-rock compositions of Tristan lavas; major element oxides in wt.%.

Sample	TDC-12-1	TDC-12-2	TDC-12-3	TDC-12-4	TDC-12-5	TDC-12-6	TDC-12-7*	TDC-12-8*	TDC-12-9	TDC-12-10
Latitude	37.067 S	37.066 S	37.067 S	37.069 S	37.066 S	37.063 S	37.064 S	37.125 S	37.122 S	37.100 S
Longitude	12.299 W	12.287 W	12.287 W	12.287 W	12.286 W	12.282 W	12.284 W	12.225 W	12.222 W	12.333 W
Age	1961 flow	15 ka	15 ka	15 ka	15 ka	81 ka	81 ka	n.d.	n.d.	n.d.
SiO_2	55.20	41.90	44.80	45.10	41.80	46.50	42.90	43.60	44.60	41.90
TiO_2	1.59	4.18	3.78	3.78	4.28	3.33	3.16	3.71	3.57	4.23
Al_2O_3	19.20	13.70	16.30	16.10	14.00	17.80	11.20	13.40	16.00	14.20
FeO_T	4.48	12.13	9.56	9.69	12.31	8.67	12.12	11.52	10.07	11.82
MnO	0.17	0.17	0.17	0.17	0.17	0.16	0.16	0.15	0.17	0.17
MgO	1.35	7.92	5.28	5.15	7.45	3.76	11.90	8.42	5.16	8.06
CaO	5.45	11.83	10.44	10.05	11.51	9.30	11.57	11.38	9.88	11.86
Na_2O	5.31	2.17	3.13	3.23	2.45	3.66	1.96	2.31	3.50	2.42
K_2O	4.82	1.58	1.99	2.56	1.72	3.00	1.51	1.79	3.11	1.49
P_2O_5	0.36	0.57	1.24	0.82	0.60	0.99	0.37	0.54	0.91	0.75
H_2O	0.47	0.94	0.95	0.95	0.86	0.58	0.39	0.49	0.45	0.36
CO_2	0.07	0.12	0.09	0.08	0.09	0.05	0.10	0.09	0.13	0.08
Sum	98.73	97.88	98.28	98.23	97.93	98.29	98.03	98.05	98.11	98.00
Mg#	34.90	53.79	49.60	48.65	51.88	43.58	63.64	56.56	47.73	54.87

Whole-rock compositions of Tristan lavas, trace elements in ppm.

Sample	TDC-12-1	TDC-12-2	TDC-12-3	TDC-12-4	TDC-12-5	TDC-12-6	TDC-12-7*	TDC-12-8*	TDC-12-9	TDC-12-10
Li	8.9	3.4	4.6	4.9	3.0	4.4	2.8	3.2	4.7	3.2
Be	2.7	1.1	1.4	1.5	1.1	1.7	0.9	1.1	1.6	1.0
Sc	2.3	30.5	16.1	16.9	28.0	10.7	36.7	31.8	17.0	28.5
Ga	21	21	20	20	21	19	19	18	23	21
V	72	378	247	256	397	183	371	366	279	352
Cr	2.3	85	1.7	10	85	10	349	177	4.3	108
Co	4.8	56	31	34	55	27	76	57	36	54
Ni	1.0	49	4.7	10.3	55	7.1	167	81	11.2	43
Rb	95	34	38	48	38	66	33	37	57	61
Cs	1.56	0.49	0.56	0.77	0.51	0.85	0.49	0.51	0.94	0.44
Sr	1231	702	1122	950	734	1110	530	778	971	804
Ba	1280	453	602	680	441	769	413	610	748	919
Zr	422	202	266	273	206	296	172	199	275	201
Nb	106	38	56	61	41	70	37	39	64	42
Y	36	25	30	30	25	32	19	23	28	24
La	141	54	74	82	56	95	48	55	86	56
Ce	290	117	162	174	121	200	100	122	178	122
Pr	28	13	17	18	14	21	11	13	19	13
Nd	99	53	72	73	56	81	43	54	73	55
Sm	15	10	13	13	10	14	7.9	10	12	10
Eu	4.3	3.0	4.0	3.8	3.2	4.1	2.4	3.0	3.7	3.2
Gd	11	8.5	11	10	8.8	11	6.5	8.2	9.9	8.6
Tb	1.42	1.06	1.32	1.31	1.09	1.36	0.82	1.01	1.22	1.07
Dy	7.71	5.83	7.08	7.00	5.99	7.42	4.55	5.57	6.74	5.73
Ho	1.37	0.97	1.19	1.22	1.01	1.27	0.77	0.95	1.15	0.98
Er	3.64	2.40	2.99	3.08	2.53	3.23	1.98	2.33	2.95	2.42
Tm	0.47	0.29	0.37	0.38	0.30	0.41	0.24	0.29	0.36	0.29
Yb	2.98	1.74	2.12	2.27	1.81	2.38	1.46	1.68	2.20	1.72
Lu	0.41	0.24	0.30	0.31	0.23	0.32	0.19	0.23	0.30	0.23
Th	18.3	6.4	8.6	10.5	6.7	11.8	5.9	6.1	10.9	6.6
U	3.30	1.19	1.59	1.94	1.25	2.23	1.04	1.15	2.02	1.03
Cu	0.99	42	13	7.9	45	8.8	77	25	24	26
Zn	104	111	108	109	114	105	101	107	114	110
Mo	5.83	2.04	2.25	3.15	1.92	3.49	1.95	1.91	3.52	2.21
Cd	0.15	0.09	0.11	0.07	0.08	0.07	0.07	0.09	0.12	0.06
Tl	0.148	0.056	0.061	0.074	0.084	0.100	0.047	0.045	0.078	0.005
Pb	7.56	2.60	3.63	2.94	2.75	3.12	2.46	2.71	4.48	0.79
Bi	0.031	0.006	0.013	0.001	0.003		0.004	0.007	0.014	
Sb	0.168	0.076	0.091	0.120	0.088	0.101	0.042	0.056	0.103	0.040

GPS coordinates are in decimal degrees based on WGS84 datum.
Ages from Hicks et al. (2014) for the same locality and rock type, but not identical sample.
FeO_T is total iron expressed as FeO.
Mg# = mol% MgO/(mol% MgO + 0.85 mol% FeO_T).
* Sample compositions are affected by cumulus olivine and pyroxene phenocrysts, see text.

0.4 mm in length, clinopyroxene, amphibole, Fe–Ti oxides and some interstitial glass.

Olivine phenocrysts in basanite are compositionally zoned with cores of uniform composition corresponding to $Fo_{75–81}$ and less magnesian rims ($Fo_{64–67}$). The concentrations of CaO and TiO_2 increase from core to rim, with 0.2 to 0.3 wt.% and 0.02 to 0.05 wt.%, respectively. Clinopyroxene phenocrysts are weakly zoned to uniform in composition, with Mg# of 75–77 in cores [$100 * X_{MgO} / (X_{MgO} + X_{FeO})$, where X_{MgO} and X_{FeO} are mole fractions]. Zoned grains of clinopyroxene have less magnesian rims, with Mg# of 69–71. The concentrations of minor constituents in crystal cores are 5–9 wt.% Al_2O_3, 1.3–5 wt.% TiO_2 and 0.3–0.5 wt.% Na_2O. In zoned clinopyroxene grains, the concentrations

Please cite this article as: Weit, A., et al., The magmatic system beneath the Tristan da Cunha Island: Insights from thermobarometry, melting models and geophysics, Tectonophysics (2016), http://dx.doi.org/10.1016/j.tecto.2016.08.010

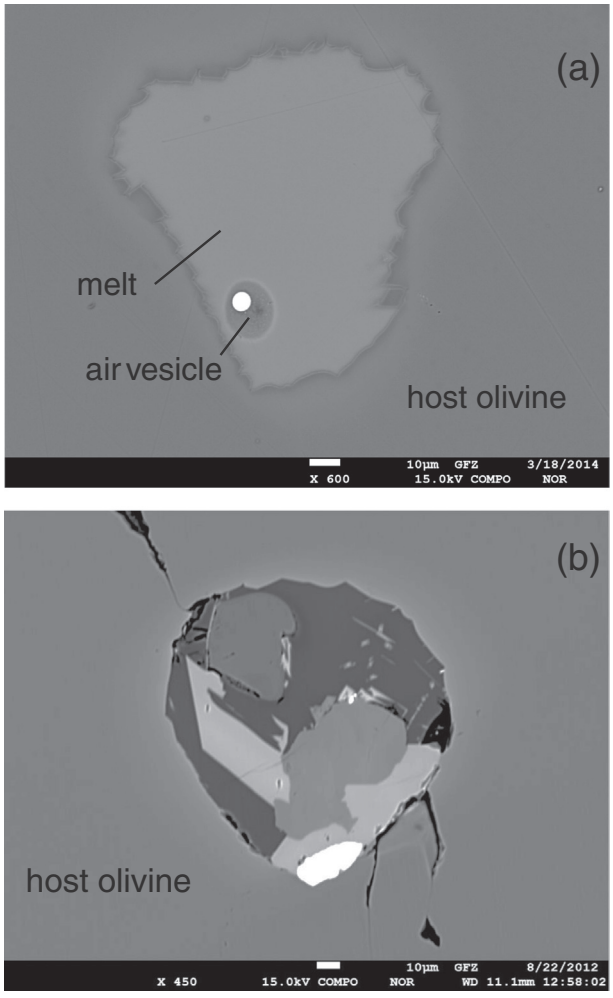

Fig. 2. Back-scatter electron micrographs of olivine-hosted melt inclusions in Tristan basanite, showing typical examples of (a) an inclusion after homogenization and (b) partially crystallized, natural inclusion.

of Al, Ti and Na tend to be higher in the rims. Plagioclase phenocrysts are typically zoned, from An_{88} in the cores to An_{70} in the rims. The concentrations of K_2O are 0.1 to 0.3 wt.% and FeO contents range from 0.5 to 0.8 wt.%. The Ti-magnetite phenocrysts contain 12–30 wt.% TiO_2, 3–9 wt.% MgO, 1.5–11 wt.% Al_2O_3 and up to 2.5 wt.% Cr_2O_3 in exceptional cases. Minor amounts of ilmenite were found in one sample. The composition of groundmass clinopyroxene crystals is similar to the phenocryst rims, at Mg# 68–71. Groundmass plagioclase, however, is more sodic than phenocryst rims, with An_{55} to An_{37}.

Plagioclase and clinopyroxene compositions in the trachyandesite sample TDC-12-1 are predictably more sodic and less magnesian than in the basanites just described. Plagioclase phenocrysts show weak, locally, oscillatory zoning with the core compositions corresponding to An_{70} and more variably sodic rims. The groundmass plagioclase compositions vary from An_{57} to An_{30}. The K_2O and FeO contents of plagioclase vary from 0.3 to 0.77 and 0.54–0.80 wt.%, respectively. Clinopyroxene phenocrysts are compositionally zoned with Mg# decreasing from 70 in cores to 56–59 in rims. The ranges of Al_2O_3 (2.7–7.9 wt.%), TiO_2 (1.1–3.3. wt.%) and Na_2O (0.5 to 1.5 wt.%) overlap with those from basanites. The groundmass Ti-magnetite is uniform in composition, with 15.9 to 16.2 wt.% TiO_2, 4.4–4.2 wt.% MgO, about 1 wt.% MnO and 0.02 wt.% Cr_2O_3.

4.2. Major-element compositions and the cumulate effect

The major element compositions of our sample suite are reported in Table 1. On the total alkali-silica (TAS) diagram (Fig. 4a) the samples plot in the alkaline field and within the range from basanites to trachy-andesite that le Roex et al. (1990) has described as a differentiation sequence related to crystal fractionation. Their least-squares fractionation model accounted for the range of magma compositions by crystallization of olivine, clinopyroxene, Fe–Ti oxides, plagioclase and minor apatite, together with amphibole and alkali feldspar in the most evolved compositions. Important to note for our study is that the most Mg-rich samples of ankaramite and basanite were shown by Le Roex et al. (1990) to be far from primitive magmas because they have low Mg# ($100 \times$ molar MgO/MgO + 0.85 FeO_{total}), and low Ni and Cr contents. Instead, they suggested that the high MgO contents of ankaramitic basanites are due to crystal accumulation. This was supported by mixing models showing that some ankaramites may contain up to 40 wt.% crystal cumulates and suggesting that the SiO_2 content in parental melts should be about 45 wt.%. In our study (Table 1) several of the basanite samples contain <45 wt.% SiO_2 and a simple mass-balance calculation of one such sample (TDC-12-2) supports the suggestion that these are partial cumulates. The composition of TDC-12-2 (with 43.3 wt.% SiO_2) is equivalent in terms of major element oxides to a mixture of a 66 wt.% melt with the composition of TDC-12-4 (46.4 wt.% SiO_2) and 34 wt.% crystals of olivine, augite, magnetite and plagioclase.

It is clear from the above that the erupted lavas experienced considerable fractionation of olivine, pyroxene and spinel during ascent and evolution, and that the most mafic samples were affected by partial crystal accumulation. The implication is that bulk-rock compositions may be a poor proxy for the melt compositions in thermobarometry calculations in some cases (see next section). Olivine partial cumulates are usually revealed by plotting forsterite content of olivine phenocrysts against whole-rock Mg# (Rhodes, 1979; Fig. 5a). Theoretically, olivine-phyric rocks formed by equilibrium crystallization should plot along the curve corresponding to the equilibrium constant of Mg–Fe olivine-melt distribution $K_D = 0.3 \pm 0.03$. Points positioned to the right of the curve imply that the whole-rock Mg# is too high and probably affected by olivine accumulation. Application of this test to our samples shows that most whole-rock compositions of ankaramitic basanite comply with the equilibrium K_D reasonably well and this holds also for the phenocrysts of clinopyroxene and plagioclase (Fig. 6). Le Roex et al. (1990) who pointed out that the mineral-melt K_D test alone is insufficient for multiple saturated melts where olivine is not the only phenocryst phase and indeed not the most abundant one. The fact that even the least-evolved Tristan lavas are multiply saturated also prevents application of inverse fractionation models to estimate primary melt compositions (e.g., Herzberg and Asimov, 2008; Lee et al., 2009). In order to resolve the uncertainty of reversing the cumulate effect, we turn to melt inclusions for an independent estimate of melt compositions.

4.3. Melt inclusions and the composition of parental melt

Melt inclusions trapped in phenocrysts during crystal growth can provide valuable information about parental melt compositions and conditions of crystallization (Sobolev, 1996). Refractory and compositionally simple minerals such as olivine are superior hosts for melt inclusions than pyroxenes or plagioclase because the potential problems of re-homogenisation and of post-entrapment modification are more tractable. Since olivine contains well-formed inclusions therefore, only olivine-hosted inclusions were investigated. Melt inclusions may undergo post-entrapment chemical modification and re-equilibration, which has to be taken into account (Danyushevsky et al., 2000). For example, FeO may be partly lost by diffusion into the olivine host (not indicated in our study) or the MgO content of inclusions may decrease because of quench crystallization of forsteritic olivine on inclusion walls at the end of homogenization run (see Mg-rims on olivine around inclusion Fig. 2a). In our case of effective but "blind" homogenization runs with many olivine grains at once, some individual inclusions may be overheated and dissolve some of the host olivine. Disequilibrium of

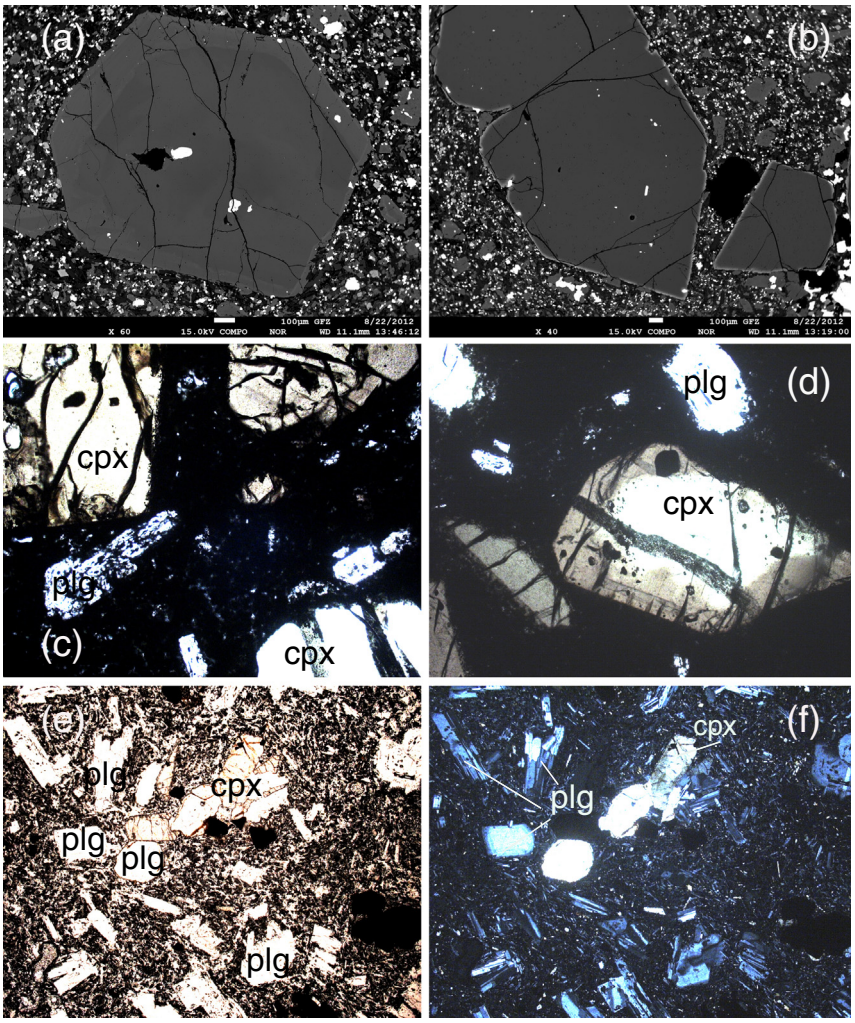

Fig. 3. Back-scatter electron micrographs showing typical examples of clinopyroxene (a) and olivine (b) phenocrysts in Tristan basanite (sample TCD-12-7), c,d) shows clinopyroxene and olivine in sample TDC 12-2 and TDC 12-8 and e,f) shows a detailed section of sample TDC 12-6 under simple polarised light (e) and under crossed nicols (f).

the included melt with olivine host can be revealed using a Rhodes diagram (Fig. 5b) in the same way as described above for the whole-rock compositions, and those compositions that were affected by post-entrapment processes can be corrected by incremental additions or subtractions of olivine normative components, e.g., as described by Danyushevsky et al. (2000).

Electron microprobe analyses of homogenized olivine-hosted melt inclusions from two samples of ankaramitic basanite are presented in Table 2. The concentrations of MgO and SiO_2 in most primitive inclusions vary in the ranges of 6.5–7 wt.% and 42–45 wt.%, respectively. These variations are similar to those observed in the most primitive whole-rock compositions (Table 1). However, a key difference between inclusions and bulk-rocks is the lower CaO contents in the inclusions (Fig. 4c) and evident in the CIPW norm projection (Fig. 7), where the rock compositions plot near the 1-atmosphere olivine–diopside–plagioclase cotectic line but the inclusions consistently offset away from the diopside corner. The difference between host rock and inclusions supports the inference made above and by Le Roex et al. (1990) that the Tristan ankaramite lavas are partial cumulates. This can be demonstrated by a simple mass-balance calculation. For example, the whole-rock composition of sample TDC-12-2 can be modelled as a mixture of olivine, augite and magnetite phenocrysts added to the average composition of melt inclusions in that sample. The mass proportions show the relative dominance of clinopyroxene (0.005 olivine:0.15 augite:0.01 magnetite:0.835 melt). Moreover, the position of melt inclusions on Fig. 7 implies that melts may have crystallized at elevated pressure, whereas the coincidence of the bulk rock compositions and 1 atmosphere cotectic melts is an artifact of crystal accumulation. Indeed, pressure estimates from clinopyroxene-melt equilibria (even using bulk rock as melt proxy) support crystallization at 0–8 to 1.2 GPa as described in Section 4.5 on geothermobarometry.

4.4. Trace elements and constraints on melt generation

The incompatible trace element contents of our sample suite are summarized in chondrite- normalized multi-element and REE diagrams (Fig. 8). These show the similarity of the new and previously-published trace element concentrations from Tristan da Cunha and there is no benefit in repeating what has been described and interpreted by le Roex et al. (1990) in terms of magma evolution. On the other hand, our study contributes a more complete set of trace elements than previous work, including the full REE spectrum. The latter allows us to examine more closely scenarios of melting depths and the degree of melting in the mantle source using the REE inverse modelling approach developed by McKenzie and O'Nions (1991, 1998). Gibson et al. (2005) used this method in a study of changing melting conditions along the Tristan plume track from the Etendeka Province, Walvis Ridge and the Gough–Tristan guyot chains. For lack of sufficient data, Tristan da Cunha was not included in that study and instead, published data from the nearby Inaccessible Island

Please cite this article as: Weit, A., et al., The magmatic system beneath the Tristan da Cunha Island: Insights from thermobarometry, melting models and geophysics, Tectonophysics (2016), http://dx.doi.org/10.1016/j.tecto.2016.08.010

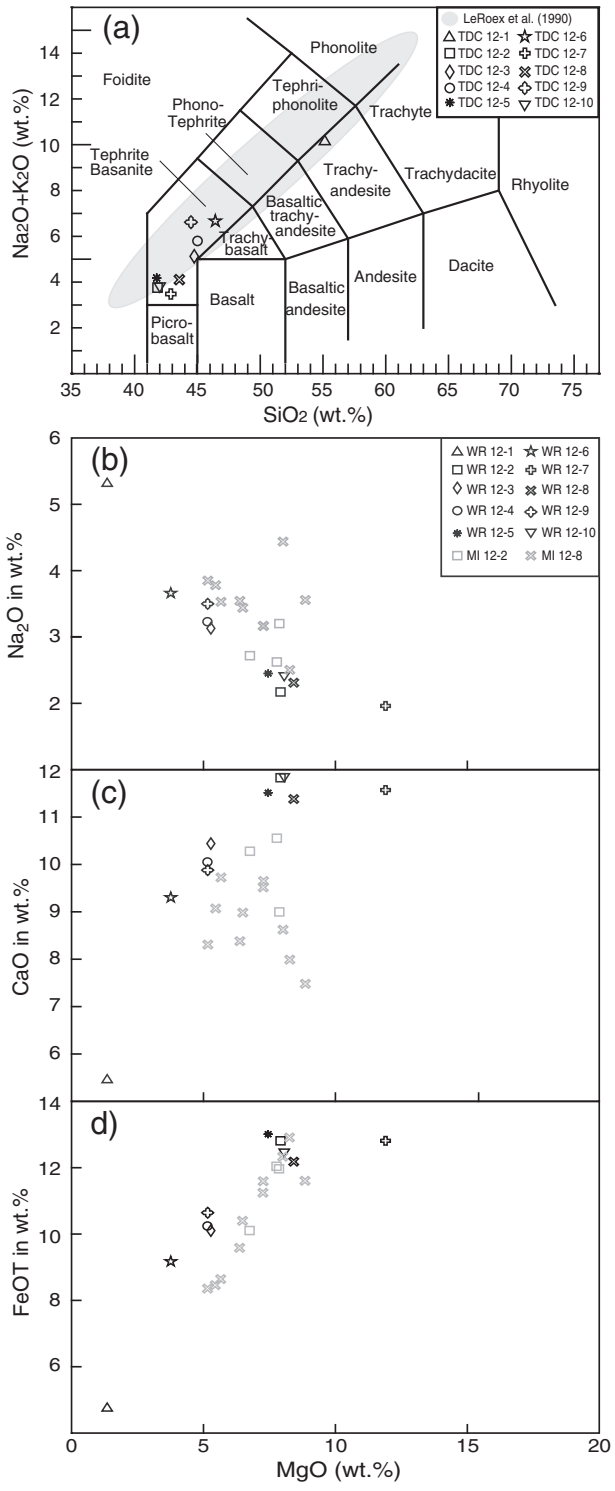

Fig. 4. Total alkali-silica (TAS) diagram showing the range of composition for Tristan lavas from Le Roex et al. (1990) in the gray field, and the samples from this study in symbols.

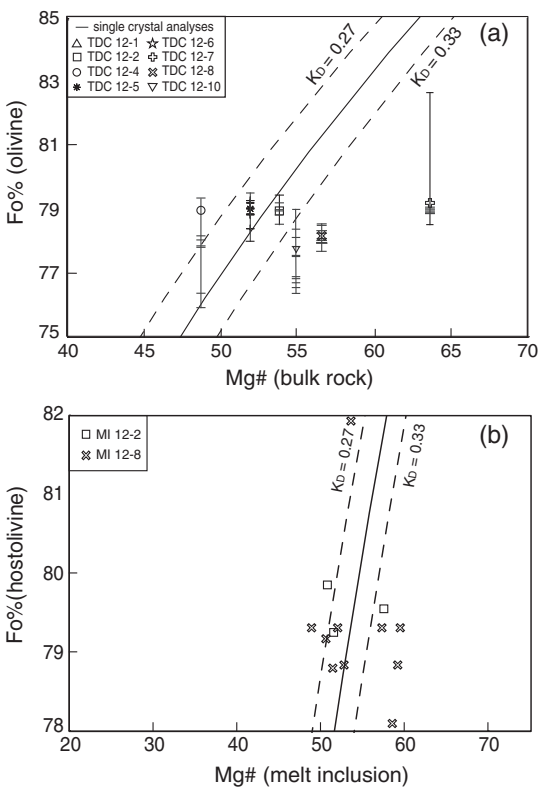

Fig. 5. The composition of olivine crystals (mol% Forsterite) compared with the Mg# (100 * molar MgO/MgO + 0.85 FeO_T) of the host-rock (a) and melt inclusions (b). Equilibrium compositions will fall near the line described by $K_D = 0.3$ (see text).

were used. Our new model for Tristan magmas also benefits from a revision of mineral-melt partition coefficients for garnet and pyroxene by Gibson and Geist (2010). It is worth mentioning that the cumulate effect noted above has minimal effect on the REE modelling because cumulus olivine and clinopyroxene contain low concentrations of these elements compared to the melt (distribution coefficients much less than one — see Gibson and Geist, 2010) and the modelling method relies most heavily on element ratios rather than abundance.

Detailed descriptions of the inverse modelling application, including a list of the mineral-melt distribution coefficients used, are given in Gibson and Geist (2010), and readers are also referred to the papers by McKenzie and O'Nions (1991) and McKenzie and O'Nions (1998) for full explanations of the method. Briefly, the model uses the incremental fractional melting scenario and calculates the concentrations of a large number of elements simultaneously. It takes advantage of the fact that the REE ratios in melts derived from a given mantle source vary in a systematic and predictable way according to both the degree of melting (reflected in LREE/MREE ratios like La/Sm) and the pressures at which melting occurs (related to the pressure dependence of garnet stability and its effect on MREE/HREE ratios like Tb/Yb). After deriving a melting scenario that satisfies the given REE constraints, the model calculates the concentrations of other incompatible trace elements based on their distribution coefficients. Correction for the effects of fractionation of olivine and clinopyroxene after melt formation employs the method of McKenzie and O'Nions (1991) based on the observed FeO* and MgO contents of the rocks. The corrected final melt fraction (Y-axis on Fig. 9c) is calculated by multiplication by $1/(1 - F)$, where F is the weight fraction of material crystallized (in our case 0.327). The models depend on knowledge or assumptions about the mantle source composition. To allow comparison with the earlier study by Gibson et al. (2005), we used the same choice of input values here as in that study. Thus, the mantle composition is chosen to represent a mixture of 25% primitive mantle and 75% depleted mantle, which fits the εNd value of 7 assigned to the common plume component FOZO (e.g., Stracke et al., 2005).

The results for Tristan basanites with MgO > 6 wt.% (5 samples: TDC 12-2, -5, -7, -8, -10) are shown in Fig. 9, where panel (a) compares the observed (average) and predicted (melt) REE concentrations, panel (b) shows the same comparison for other incompatible elements and panel (c) shows the calculated melt fraction vs. depth of melting curves (with and without fractionation correction). The dashed lines show

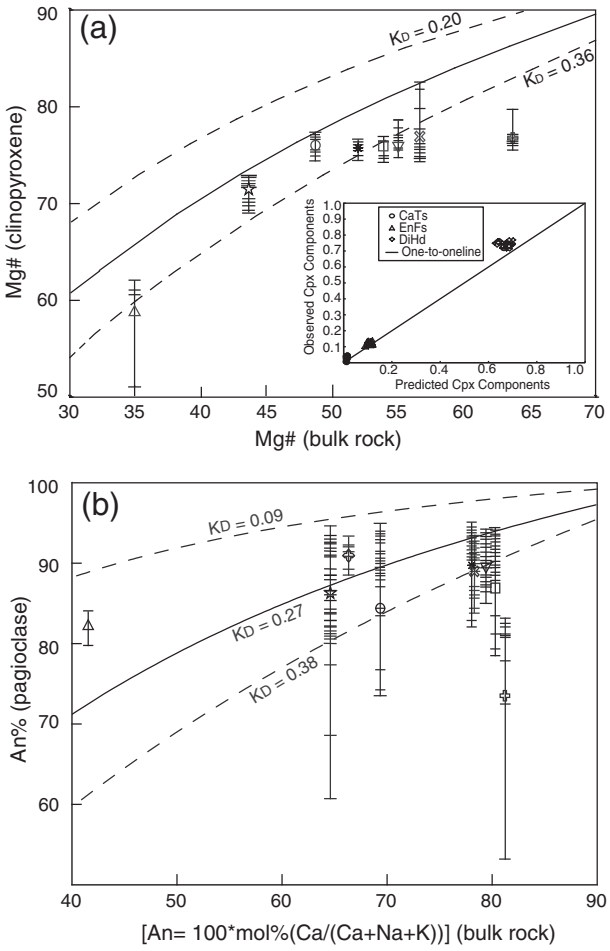

Fig. 6. The composition of clinopyroxene crystals (Mg#) compared with the Mg# of the host rock (a) and the composition of plagioclase crystals (An%) compared to An% of the host rock (b). Equilibrium compositions for clinopyroxene fall near $K_D = 0.28$ and for plagioclase near $K_D = 0.27$.

predicted adiabatic decompression melting for a range of mantle potential temperatures. It can be seen in Fig. 9c that the fractionation correction (solid line) closely follows the predicted slope of adiabatic decompression melting. Taken together, the modelling results suggest that Tristan basanites reflect low-degree (<5%) partial melts generated by adiabatic decompression that started in the garnet peridotite field and extended to about 60 km depth, which may be interpreted as the

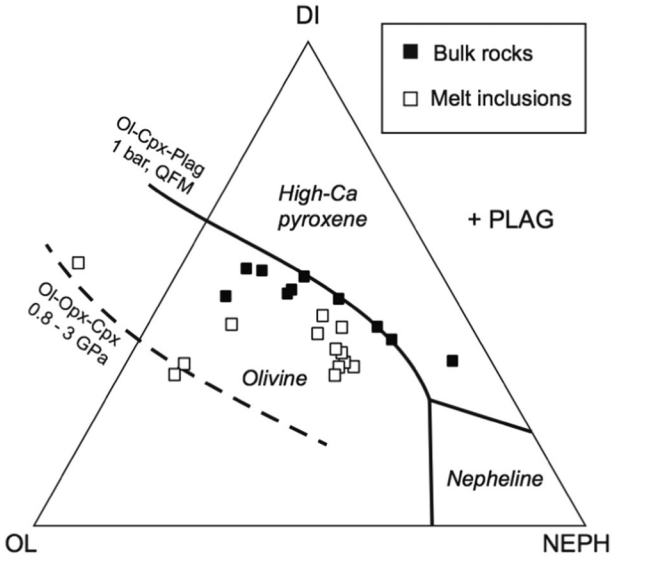

Fig. 7. Comparison of the CIPW normative composition of Tristan bulk-rocks and melt inclusions in the olivine–diopside–nepheline–plagioclase system with experimental cotectic melt compositions at 1 bar and 8–30 kbar from Sack et al. (1987).

lithosphere–asthenosphere boundary at this position. In order to fit the elevated concentrations of strongly incompatible trace elements a low-fraction melt tail extending to depths of ~140 km is required. We suggest that this represents 'deep' incipient melting of a volatile-rich component in the upwelling plume. Most melt is generated between about 80 and 60 km, and this part of the melting curve is consistent with decompression melting at a potential temperature near 1350 °C. There is good agreement between this value and the maximum potential temperature of 1358 °C estimated from the thermobarometry calculations discussed in Section 4.5 below.

The inverse modelling provides a good fit to most incompatible trace elements except Pb (Fig. 9b). This misfit was also noticed in the models for Inaccessible melts by Gibson et al. (2005) who proposed that the low Pb was caused by melting of a source consisting of ~20% of delaminated metasomatised sub-continental lithospheric mantle and 80% of plume mantle.

4.5. Thermobarometry

Estimations of crystallization temperatures and pressures are based on mineral-melt equilibria formulations reviewed by Putirka (2008). In

Table 2
Compositions of homogenized melt inclusions (MI) in olivine phenocrysts.

Sample	TDC-12-2			TDC-12-8									
MI	2–1	2–2	2–3	8–1	8–2	8–3	8–4	8–5	8–6	8–7	8–8	8–9	8–10
SiO_2	41.91	42.99	42.04	45.02	44.68	46.98	44.43	42.91	45.51	45.53	44.87	42.79	45.80
TiO_2	4.12	4.41	4.16	3.41	3.31	3.73	3.22	3.60	3.64	3.69	3.20	4.28	3.49
Al_2O_3	14.49	15.09	15.29	16.19	15.79	14.97	13.73	15.27	16.27	16.48	16.00	15.77	15.97
Fe_2O_3*	2.60	2.26	2.55	2.03	2.40	2.05	2.68	2.52	1.98	2.16	2.28	2.45	1.99
FeO*	11.31	9.75	11.17	8.50	10.21	9.35	11.47	12.33	8.35	9.78	10.95	10.79	8.40
MnO	0.12	0.11	0.19	0.13	0.17	0.16	0.22	0.18	0.18	0.19	0.23	0.13	0.14
MgO	6.77	7.43	6.49	7.02	5.50	7.06	7.00	7.11	6.81	6.15	7.12	6.43	6.67
CaO	10.90	10.11	9.39	9.39	10.03	8.25	8.91	8.30	8.76	9.10	7.89	9.92	7.99
Na_2O	2.70	2.66	3.33	3.39	3.33	3.47	4.57	2.59	3.63	3.47	3.74	3.24	3.68
K_2O	2.20	2.73	2.66	2.85	2.60	1.63	1.53	2.56	2.83	1.80	1.39	2.30	3.20
Cl	0.05	0.06	0.06	0.05	0.04	0.00	0.02	0.00	0.07	0.01	0.00	0.06	0.06
Total	97.16	97.61	97.33	97.97	98.06	97.65	97.78	97.37	98.04	98.35	97.67	98.15	97.40
Fo# Host	79.3	79.6	79.8	79.3	79.3	79.3	79.3	79.2	78.8	78.8	81.9	78.8	78.1
Mg# MI	51.6	57.6	50.9	59.6	48.99	57.4	52.1	50.7	59.2	52.9	53.7	51.5	58.6

Mg# = mol%MgO/(mol%MgO + 0.85mol%FeO*).
FeO* is total iron expressed as FeO.
* Ferric–ferrous ratio calculated using the Kress and Carmichael (1991) equation at 1200 °C and fO_2 equal to that of the QFM buffer. Fo# = forsterite percentage in host olivine.

Please cite this article as: Weit, A., et al., The magmatic system beneath the Tristan da Cunha Island: Insights from thermobarometry, melting models and geophysics, Tectonophysics (2016), http://dx.doi.org/10.1016/j.tecto.2016.08.010

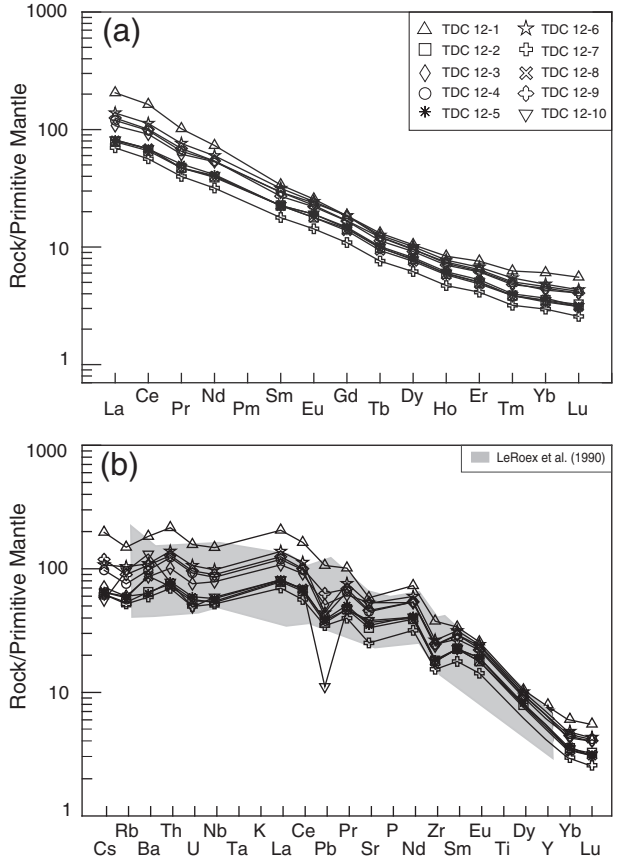

Fig. 8. Primitive-mantle normalized trace element concentrations in Tristan samples from this study, showing good correspondence with the shaded field of data from Le Roex et al. (1990).

the Tristan samples, olivine and clinopyroxene crystals have very uniform core compositions and we therefore use the average of electron microprobe core analyses for each sample in the calculations (Table 3). For the choice of nominal melt compositions we used two approaches. The first and preferred one is the melt inclusion compositions. Inclusions were studied and analysed only in olivine hosts for reasons described above (Section 4.3), but we believe the melt compositions are relevant for clinopyroxene-melt equilibrium as well, because the inclusions contain daughter crystals of clinopyroxene (Fig. 2b), all samples contain abundant clinopyroxene and olivine phenocrysts with textures suggesting simultaneous crystallization, and MELTS calculations (Ghiorso and Sack, 1995) using the inclusion compositions predict that both phenocryst phases are on the liquidus at the same temperature. The second approximation of melt composition is simply to use the whole-rock composition in samples, but avoiding those that are most strongly affected by cumulus minerals (marked with asterisk in Table 1).

Additional input for the calculations require approximations or assumptions. The ferrous–ferric iron ratio in the melt phase was calculated using the equation of Kress and Carmichael (1991) assuming fO_2 corresponding to the QFM buffer. For a temperature of 1200 °C, the resulting ratio of $FeO/(FeO + Fe_2O_3)$ is about 0.85. Water contents in the original melt are difficult to constrain. Measured water and CO_2 concentrations in the bulk rocks are low, from 0.4 to 0.9 wt.% and 0.05 to 0.13 wt.%, respectively (Table 1). However, some volatile loss during differentiation and eruption is likely if not certain, and we note that the melt inclusions have analytical totals between about 97 and 98 wt.% (Table 2), suggesting higher volatile contents in the parental melts. An extensive compilation of OIB glass and melt inclusion data by Kovalenko et al. (2007) suggest low water contents of about 0.5 wt.%. For lack of a reliable value of initial H_2O content in the parental melt we assumed 1 wt.% in the calculations. A sensitivity test showed a downward shift of about 50 °C in temperature for each additional 1 wt.% H_2O.

The olivine-melt temperatures were calculated from equation 22 of Putirka (2008), which is based on the formulation of Beattie (1993) with added terms for pressure and melt H_2O dependencies. The pressure input for these calculations are those of clinopyroxene barometry, which is justified by the coexistence of clinopyroxene and olivine in all samples. Putirka (2008) determined an uncertainty of ±43 °C for Eq. (22). Clinopyroxene-melt equilibria yield estimates for both temperature and pressure. We employed iterative simultaneous solution for pressure and temperature using equation 30 in Putirka (2008), for which the given uncertainties are ±45 °C and ±0.36 GPa. The trachyandesite sample TDC-12-1 lacks olivine, and in this case we used the plagioclase-melt thermometer defined by equation 24a in Putirka (2008) in addition to the clinopyroxene-melt thermobarometer described above. The temperature uncertainty for equation 24a is ±36 °C. For that sample, too, because of its evolved compositions, we used the clinopyroxene-melt thermobarometer of Masotta et al. (2013) which was calibrated by new experimental data for trachytes and phonolites at 0.05 to 1.5 GPa (uncertainties are ±18 °C and 0.12 GPa for this limited range). All thermobarometry results are listed in Table 4 and summarized below.

The trachyandesite from the 1961 lava (TDC-12-1) yielded lower P–T estimates as expected from its more evolved composition. Clinopyroxene thermobarometry using Putirka (2008, Eq. (30)) yielded 979 °C and 0.16 GPa. The calibration of Masotta et al. (2013) yields higher temperature and pressure conditions (1000 °C and 0.35 GPa, resp.), but the two calibrations agree within the large uncertainties of ±45 °C and 0.37 GPa estimated for the Putirka (2008) calibrations. An independent temperature estimate based on plagioclase-melt equilibria from the same sample (TDC-12-1) is 1089 °C, slightly higher than either of the two clinopyroxene estimates but within the method uncertainties.

The basanite samples yielded olivine-melt temperatures in the total range from 1153° to 1269 °C; however only 2 of 18 values are below 1200 °C. In samples where temperatures from melt inclusions and bulk rock can be compared, the results overlap in one case (TDC-12-2) whereas bulk-rock temperatures are about 30° higher in another (TDC-12-8). The latter probably relates to the partial cumulate nature of the bulk rock. The clinopyroxene-melt calculations for basanite samples suggest pressure and temperature ranges of 1153 to 1249 °C and 0.7–1.3 GPa, respectively. The values calculated from melt inclusions are again slightly lower than those with bulk-rock data, but the maximum difference is 50 °C and 0.2 GPa. The positive correlation of calculated P–T values and MgO contents of the nominal melt compositions means that if crystal accumulation significantly increases the bulk-rock MgO beyond the true melt composition, the highest calculated P–T values may be unreliable. The example where bulk-rock composition is most strongly affected by cumulates (not on Table 3 for that reason) is sample TDC-12-7 with 11.9 wt.% MgO, which would yield 1312 °C and 1.7 GPa. Comparing olivine-melt and pyroxene-melt temperatures from the same samples (Table 4) we find that the former is commonly higher by 20–50 °C. There is no petrographic evidence in the rocks that clinopyroxene formed later than olivine, and MELTS crystallization modelling suggest that both minerals are coeval. The temperature difference is more likely related to the uncertainties of the mineral-melt thermometers and the assumptions inherent in their use (e.g., H_2O contents, fO_2).

For comparison with other hotspot islands and concepts of mantle plumes it is useful to estimate the potential temperature of the Tristan mantle source. The potential temperature is the temperature the mantle source would have at the surface if it rose from the melting depth adiabatically and without melting (e.g. Putirka, 2008). The conversion of melt temperature to potential temperature accounts for the latent

heat of melting, which requires estimating the degree of melting; and for the adiabatic rise, which requires knowledge of the initial melting depth. Both of those estimates were derived from the REE inversion model, which suggests 5% melting and ca. 80 km depth (Fig. 9c, neglecting the small-volume deeper tail). For consistency with the thermobarometry calibrations, we used the formulation of Putirka (2008) for calculating Tp from a known melt temperature, pressure and melt fraction. For the temperature value we use a maximum olivine-melt temperature for basanite (1250 °C) as the closest approach in our study to primitive melting conditions (but still a minimum since Tristan basanites are not primary melts). Taking the pressure equivalent of 80 km to be 2.7 GPa, the Tp calculation yields a value of 1363 °C (calculation details in Putirka, 2008). This is in good agreement with the modelled melt–depth curve and isotherms in Fig. 9c.

5. Discussions

5.1. Comparison with geophysical results from the Tristan group islands

Geissler et al. (2016) describe the results of a teleseismic study based on seismometer stations on Tristan da Cunha (station TRIS) and Nightingale Island (NIG01) and an array of ocean-bottom seismometers deployed around the Tristan group islands. Of relevance to this paper are the estimations of the Moho depth and the lithospheric thickness in this region, which helps put the depths of magma generation, storage and crystallization into a geodynamic context. For this purpose, the S-wave velocity structure of the crust and uppermost mantle was constrained from Ps receiver functions (P–S converted waves, see Geissler et al., 2016, for details). The results from ocean-bottom stations suggest a normal crustal thickness near 7 km but the island-based stations record thicker crust and a more complex velocity structure. Station TRIS, located near the site of the 1961 eruption at the edge of the island, yielded an S-wave velocity model with a Moho depth of ca. 9 km, whereas station NIG01 on Nightingale Island yielded a complex velocity structure (Fig. 10) with typical upper-mantle velocities below 19 km and a complex "Moho zone" between 18 and 6 km with periodic velocity changes which Geissler et al. (2016) related to magmatic intrusions. The difference in crust and mantle S-wave velocity structures between the neighboring islands is potentially an artifact of the array geometry. The TRIS station is situated at the edge of the island and most observation points (piercing points) of the teleseismic events are on the island flanks and seafloor. The geometric situation at NIG01 on Nightingale is more favorable because the observation points lie directly beneath the island and the crustal coverage is better. With some uncertainty, we suggest that the greater crustal thickness beneath Nightingale may also pertain to the neighboring islands of Tristan da Cunha and Inaccessible.

Our pressure estimates for first crystallization of the basanite magmas are from 0.8 to 1.3 GPa (Table 4), which are equivalent to 24 to 36 km depth for the crustal density of 3 g/cm^3 based on the density of basalt, the dominant component of the island (Okrusch and Matthes, 2014). These petrological estimates of magma storage depth are below the Moho estimated from seismologic results of Geissler et al. (2016). In contrast, the pressure estimated for trachyandesite TDC-12-1 (0.16–0.35 GPa) suggests crystallization conditions for the evolved magmas in the Tristan lower crust (6 to 10 km). These results in general support the idea (Geissler et al., 2016) that a zone near the Moho with magma intrusion and storage can explain the velocity variations at 6–19 km in the NIG01 model (Fig. 10), but our results indicate that initial crystallization of the Tristan basanite magmas took place significantly below that depth.

It is not clear what would cause the stagnation of mantle-derived melts below the Moho, but we note that several thermobarometric studies of crystallization depths under the Canary Islands also proposed a magma storage zone in lithosphere at depths similar to our estimate for Tristan (Klügel et al., 2005, 2015; Longpré et al., 2008; Stroncik

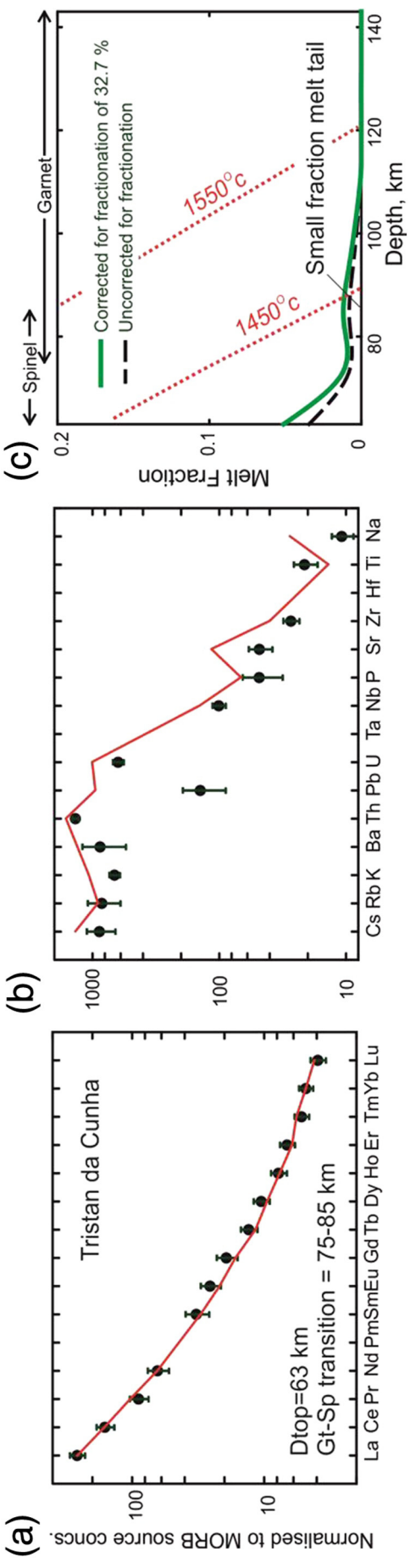

Fig. 9. Results of REE inversion models for Tristan basanites: (a) comparing model fit (solid line) to observed REE contents (average for samples >6 wt.% MgO with vertical bar giving 1 standard deviation); (b) comparing model fit to observed incompatible trace elements, with symbols as in (a); (c) degree-of-melting vs. melting depth model compared with adiabatic decompression melt curves at variable potential temperature. Solid and dashed curves show results corrected and not corrected for magma fractionation. See text.

Table 3
Summary of mineral core compositions in samples used for thermobarometry.

Olivine

Sample		SiO_2	TiO_2	Al_2O_3	FeO	MnO	MgO	CaO	NiO	Cr_2O_3	Total
TDC 12-2	Mean	38.99	0.03	0.04	19.73	0.27	41.44	0.31	0.04	0.01	100.86
	Std. Dev.	0.45	0.02	0.01	0.16	0.08	0.16	0.02	0.03	0.01	0.50
	N	50	50	50	50	50	50	50	50	50	50
TDC 12-4	Mean	38.57	0.03	0.04	20.54	0.35	40.19	0.32	0.02	0.00	100.05
	Std. Dev.	0.27	0.02	0.01	0.94	0.05	0.87	0.02	0.02	0.01	0.26
	N	27	27	27	27	27	27	27	27	27	27
TDC 12-5	Mean	38.95	0.03	0.04	19.66	0.26	41.22	0.31	0.04	0.01	100.52
	Std. Dev.	0.26	0.01	0.01	0.29	0.09	0.31	0.02	0.03	0.01	0.35
	N	32	32	32	32	32	32	32	32	32	32
TDC 12-8	Mean	38.98	0.03	0.03	20.38	0.31	40.90	0.28	0.05	0.01	100.98
	Std. Dev.	0.24	0.02	0.01	0.24	0.08	0.27	0.01	0.02	0.01	0.32
	N	48	48	48	48	48	48	48	48	48	48
TDC 12-10	Mean	38.75	0.03	0.03	20.82	0.37	39.88	0.25	0.04	0.01	100.18
	Std. Dev.	0.24	0.02	0.01	0.80	0.09	0.80	0.23	0.03	0.01	0.30
	N	43	43	43	43	43	43	43	43	43	43

Clinopyroxene

Sample		SiO_2	Al_2O_3	K_2O	Cr_2O_3	CaO	TiO_2	Na_2O	MgO	FeO	MnO	Total
TDC 12–1	Mean	47.34	5.47	0.02	0.01	22.15	2.22	0.79	10.66	11.24	0.61	100.51
	Std. Dev.	2.41	1.91	0.02	0.01	0.57	1.08	0.39	1.38	1.71	0.44	0.47
	N	12.00	12.00	12.00	12.00	12.00	12.00	12.00	12.00	12.00	12.00	12.00
TDC 12-2	Mean	46.14	7.59	0.00	0.00	22.47	2.96	0.44	13.13	7.46	0.10	100.29
	Std. Dev.	0.61	0.63	0.00	0.01	0.24	0.30	0.04	0.24	0.20	0.05	0.30
	N	68.00	68.00	68.00	68.00	68.00	68.00	68.00	68.00	68.00	68.00	68.00
TDC 12-4	Mean	46.32	7.01	0.00	0.00	22.33	3.00	0.42	13.32	7.41	0.11	99.93
	Std. Dev.	1.05	1.05	0.00	0.01	0.17	0.32	0.04	0.48	0.28	0.05	0.35
	N	45.00	45.00	45.00	45.00	45.00	45.00	45.00	45.00	45.00	45.00	45.00
TDC 12-5	Mean	45.74	7.50	0.00	0.00	22.40	2.97	0.44	13.14	7.53	0.11	99.83
	Std. Dev.	0.81	0.80	0.00	0.01	0.20	0.27	0.05	0.38	0.25	0.05	0.35
	N	74.00	74.00	74.00	74.00	74.00	74.00	74.00	74.00	74.00	74.00	74.00
TDC 12-6	Mean	46.92	6.95	0.01	0.01	22.29	3.20	0.45	12.38	8.01	0.14	100.34
	Std. Dev.	1.10	1.05	0.01	0.01	0.18	0.43	0.05	0.46	0.26	0.02	0.39
	N	47.00	47.00	47.00	47.00	47.00	47.00	47.00	47.00	47.00	47.00	47.00
TDC 12-7	Mean	46.79	6.94	0.00	0.02	22.43	2.32	0.41	13.55	7.45	0.09	100.01
	Std. Dev.	0.73	0.65	0.00	0.05	0.21	0.31	0.05	0.43	0.30	0.04	0.40
	N	70.00	70.00	70.00	70.00	70.00	70.00	70.00	70.00	70.00	70.00	70.00
TDC 12-8	Mean	47.32	6.95	0.00	0.03	22.30	2.31	0.46	13.72	7.18	0.08	100.35
	Std. Dev.	1.44	1.12	0.00	0.12	0.30	0.60	0.05	0.89	0.65	0.05	0.31
	N	67.00	67.00	67.00	67.00	67.00	67.00	67.00	67.00	67.00	67.00	67.00
TDC 12-10	Mean	45.76	7.94	0.00	0.01	22.37	2.84	0.44	13.31	7.36	0.09	100.13
	Std. Dev.	0.73	0.63	0.00	0.02	0.19	0.35	0.04	0.38	0.24	0.05	0.38
	N	62.00	62.00	62.00	62.00	62.00	62.00	62.00	62.00	62.00	62.00	62.00

Plagioclase

Sample		SiO_2	Al_2O_3	K_2O	CaO	BaO	Na_2O	MgO	FeO	Total
TDC 12-1	Mean	51.15	31.31	0.32	13.74	0.14	3.30	0.06	0.55	100.57
	Std. Dev.	0.66	0.48	0.04	0.45	0.02	0.21	0.01	0.03	0.21
	N	3.00	3.00	3.00	3.00	3.00	3.00	3.00	3.00	3.00

Mean value, standard deviation and number of analyses. Full data are given in the electronic supplement.

et al., 2009; Barker et al., 2015). Our REE inversion models for Tristan and the earlier results for Inaccessible Island suggest that the melting column has a consistent top depth of about 60 km. This is good agreement with the new seismologic estimates for the lithospheric thickness of 65–70 km by Geissler et al. (2016) and close to the 56 km derived from the standard plate cooling model (Humphreys and Niu, 2009). Our thermobarometry results, and those from several other hotspot islands in the Atlantic described by Klügel et al. (2015) show that magma passes about half-way through the lithosphere before initial stagnation and crystallization in about 30 km depth.

6. Conclusions

The results of petrologic and geochemical studies on a suite of crystal-rich ankaramite–basanite samples collected from Tristan da Cunha provide estimates of magmatic crystallization temperatures and pressures. We confirm the suggestion of Le Roex et al. (1990) that most Mg-rich ankaramite samples are affected by crystal accumulation and do not represent melt compositions. Olivine-hosted melt inclusions from these rocks provide better information on the melt composition. Thermobarometry calculations from olivine-melt and clinopyroxene-melt equilibrium pairs yielded consistent temperature estimates of 1200–1250 °C and 0.8–1.3 GPa for the basanite magmas. The range of temperatures calculated from bulk-rock and melt inclusions overlap, with the bulk-rock data at the high-temperature range. The pressure estimates from these rocks imply a depth of magma storage and crystallization on the order of 24–36 km beneath the island. Comparison with Moho depths derived from a companion geophysical study of the Tristan hotspot show that this zone of magma storage is in the uppermost mantle. Significantly lower temperature–pressure conditions of 980–1100 °C and 0.2 to 0.35 GPa were obtained from clinopyroxene and plagioclase geothermobarometry for a sample from lava erupted in 1961. The inferred crystallization depth of 6–10 km for this magma is in the base of the crust and probably represents a level of magma differentiation.

Please cite this article as: Weit, A., et al., The magmatic system beneath the Tristan da Cunha Island: Insights from thermobarometry, melting models and geophysics, Tectonophysics (2016), http://dx.doi.org/10.1016/j.tecto.2016.08.010

Table 4
Thermobarometry results obtained using mineral-melt thermometers and barometers.

Sample	Melt*	Olivine-melt	Clinopyroxene-melt		Plagioclase-melt
		T, °C	T, °C	P, GPa	T, °C
TDC-12-1	WR	No olivine	979/1000**	0.2	1089
TDC-12-2	WR	1249	1235	1.2	
	MI 2-1	1225	1212	1.2	
	MI 2-2	1247	1190	1.1	
	MI 2-3	1220	1189	1.3	
TDC-12-4	WR	1153	1153	0.7	
TDC-12-5	WR	1237	1217	1.1	
TDC-12-6	WR	No olivine	1107	0.5	
TDC-12-8	WR	1269	1249	1.3	
	MI 8-1	1238	1190	1.0	
	MI 8-2	1179	1166	0.8	
	MI 8-3	1236	1194	1.0	
	MI 8-4	1241	1186	1.0	
	MI 8-5	1237	1185	1.3	
	MI 8-6	1235	1180	1.0	
	MI 8-7	1202	1169	0.9	
	MI 8-8	1230	1172	1.1	
	MI 8-9	1211	1177	1.0	
	MI 8-10	1238	1174	1.1	
TDC-12-9	WR	No olivine	1163	0.9	
TDC-12-10	WR	1259	1232	1.2	

Olivine-melt temperatures from Putirka (2008, Eq. (22)); clinopyroxene-melt temperatures and pressures from Putirka (2008, Eq. (30)) except values ** from Masotta et al. (2013). Plagioclase-melt temperatures from Putirka (2008, Eq. (24a)).
For the MI temperatures, we used the composition of the corresponding olivine host crystal; for WR temperatures we used the mineral average compositions from Table 3.
* Nominal melt composition used: WR — whole rocks from Table 1; MI — melt inclusions from Table 2.

The trace element data from Tristan basanites provide new constraints on the depth and degree of melting in the mantle source. Results from REE inverse modelling of these data imply 5% melt fraction generated from a melting column with its base at 80–100 km and a top at 60 km, which is similar to results from nearby Inaccessible Island (Gibson et al., 2005) and consistent with a lithospheric thickness estimated from cooling models. The combination of melting models and our crystallization temperatures suggests a mantle potential temperature of about 1360 °C for the Tristan hotspot.

Acknowledgements

We are grateful to the people of Tristan and the island administration for permission to work on the island, for hospitality and help in sample collection. We thank Captain Ralf Schmidt, the crew of R/V Maria S. Merian and the Scientific Party of cruise MSM20/2 for their skilled and friendly work in support of this study. Oona Appelt (Potsdam) provided expert support for the microprobe analyses. Constructive reviews by Sverre Planke and Abigail Barker helped improve the paper. This work was supported with funding by the Deutsche Forschungsgemeinschaft DFG in the framework of the priority program SPP-1375 "SAMPLE".

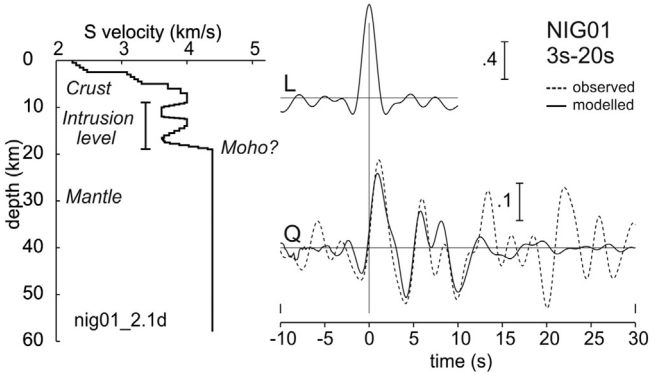

Fig. 10. S-wave velocity–depth profiles derived from waveform modelling of Ps receiver function at the temporary station NIG01 on Nightingale Island. The model 2.1d (see Geissler et al., 2016 details) fits waveform (trace Q)ms up to ~12 s delay time and indicates a Moho depth at ~19 km with a complex velocity structure which may indicate intrusion/storage levels of magma (see text). The scale bars denote signal amplitudes relative to the primary deconvolved P-phase (L trace).

Appendix A. Supplementary data

Supplementary data to this article can be found online at http://dx.doi.org/10.1016/j.tecto.2016.08.010.

References

Baker, P.E., Gass, I.G., Harris, P.G., Le Maitre, R.W., 1962. The volcanological report of the Royal Society expedition to Tristan da Cunha, 1962. Philos. Trans. A 256, 439–575.
Barker, A.K., Troll, V.R., Carracedo, J.C., Nicholls, P.A., 2015. The magma plumbing system for the 1971 Teneguía eruption on La Palma, Canary Islands. Contrib. Mineral. Petrol. 170, 54.
Beattie, P., 1993. Olivine-melt and orthopyroxene-melt equilibria. Contrib. Mineral. Petrol. 115, 103–111.
Danyushevsky, L.V., Della-Pasqua, F.N., Sokolov, S., 2000. Re-equilibration of melt inclusions trapped by magnesian olivine phenocrysts from subduction-related magmas: petrological implications. Contrib. Mineral. Petrol. 138, 68–83.
Dulski, P., 2001. Reference materials for geochemical studies: new analytical data by ICP-MS and critical discussion of reference values. Geostand. Newslett. 25, 87–125.
Ewart, A., Milner, S.C., Armstrong, R.A., Duncan, A.R., 1998. Etendeka volcanism of the Goboboseb Mountains and Messum Igneous Complex, Namibia. Part I: geochemical evidence of early cretaceous tristan plume melts and the role of crustal contamination in the Parana–Etendeka CFB. J. Petrol. 39, 191–225.
Ewart, A., Marsh, J.S., Milner, S.C., Duncan, A.R., Kamber, B.S., Armstrong, R.A., 2004. Petrology and geochemistry of early cretaceous bimodal continental flood volcanism of the NW Etendeka, Namibia. Part 1: introduction, mafic lavas and re-evaluation of mantle source components. J. Petrol. 45, 59–105.
Geissler, W.H., Jokat, W., Jegen, M., Baba, K., 2016. Thickness of the oceanic crust and the mantle transition zone in the vicinity of the Tristan da Cunha hot spot estimated from ocean-bottom and ocean-island seismometer receiver functions. Tectophysics this volume.
Ghiorso, M.S., Sack, R.O., 1995. Chemical mass transfer in magmatic processes IV. A revised and internally consistent thermodynamic model for the interpolation and extrapolation of liquid–solid equilibria in magmatic systems at elevated temperatures and pressures. Contrib. Mineral. Petrol. 119, 197–212.
Gibson, S.A., Geist, D., 2010. Geochemical and geophysical estimates of lithospheric thickness variation beneath Galápagos. Earth Planet. Sci. Lett. 300, 275–286.
Gibson, S.A., Thompson, R.N., Day, J.A., Humphris, S.E., Dickin, A.P., 2005. Melt-generation processes associated with the Tristan mantle plume: constraints on the origin of EM-1. Earth Planet. Sci. Lett. 237, 744–767.
Harris, C., Smith, H.S., Le Roex, A.P., 2000. Oxygen isotope composition of phenocrysts from Tristan da Cunha and Gough island lavas: variation with fractional crystallization and evidence for assimilation. Contrib. Mineral. Petrol. 138, 164–175.
Hawkesworth, C.J., Kelley, S., Turner, S., Le Roex, A., Storey, B., 1999. Mantle processes during Gondwana break-up and dispersal. J. Afr. Earth Sci. 28, 239–261.
Herzberg, C., Asimov, P.D., 2008. Petrology of some oceanic island basalts: PRIMELT2.XLS software for primary magma calculation. Geochem. Geophys. Geosyst. 9. http://dx.doi.org/10.1029/2008GC002057.
Hicks, A., Barclay, J., Mark, D.F., Loughlin, S., 2012. Tristan da Cunha: constraining eruptive behavior using the $^{40}Ar/^{39}Ar$ dating technique. Geology 40, 723–726.
Hoernle, K., Rohde, J., Hauff, F., Garbe-Schoenberg, D., Homrighausen, S., Werner, R., Morgan, J.P., 2015. How and when plume zonation appeared during the 132 Myr evolution of the Tristan Hotspot. Nat. Commun. 6, 7799. http://dx.doi.org/10.1038/ncomms8799.
Humphreys, E.R., Niu, Y., 2009. On the composition of ocean island basalts (OIB): the effects of lithospheric thickness variation and mantle metasomatism. Lithos 112, 118–136.
Klügel, A., Hansteen, T.H., Galipp, K., 2005. Magma storage and underplating beneath Cumbre Vieja volcano, La Palma (Canary Islands). Earth Planet. Sci. Lett. 236 (1–2), 211–226 (30 July 2005).
Klügel, A., Longpré, M.A., García-Cañada, L., Stix, J., 2015. Deep intrusions, lateral magma transport and related uplift at ocean island volcanoes. Earth Planet. Sci. Lett. 431, 140–149 (1 December 2015).
Kovalenko, V.I., Naumov, V.B., Girnis, A.V., Dorofeeva, V.A., Yarmolyuk, V.V., 2007. Volatiles in basaltic magmas of ocean islands and their mantle sources: I. Melt compositions deduced from melt inclusions and glasses in the rocks. Geochem. Int. 45, 105–122.
Kress, V.C., Carmichael, I.S.E., 1991. The compressibility of silicate liquids containing Fe_2O_3 and the effect of composition, temperature, oxygen fugacity and pressure on their redox states. Contrib. Mineral. Petrol. 82–92.
Le Roex, A.P., Cliff, R.A., Adair, B.J.I., 1990. Tristan da Cunha, South Atlantic: geochemistry and petrogenesis of a basanite–phonolite lava series. J. Petrol. 31, 779–812.
Lee, C.-T.A., Luffi, P., Plank, T., Dalton, H., Leeman, W.P., 2009. Constraints on the depths and temperatures of basaltic magma generation on earth and other terrestrial planets using new thermobarometers for mafic magmas. Earth Planet. Sci. Lett. 279, 20–33.

Longpré, M.A., Hansteen, T.H., Troll, V.R., 2008. Upper mantle magma storage and transport under a Canarian shield-volcano, Teno, Tenerife (Spain). J. Geophys. Res. Solid Earth 113, B08203.
Masotta, M., Moore, G., Gaeta, M., Freda, C., Mollo, S., 2013. Clinopyroxene-liquid thermometers and barometers specific to alkaline differentiated magmas. Contrib. Mineral. Petrol. 166, 1545–1561.
McKenzie, D., O'Nions, R.K., 1991. Partial melt distribution from inverstions of rare earth element concentrations. J. Petrol. 32, 1021–1091.
McKenzie, D., O'Nions, R.K., 1998. Melt production beneath oceanic islands. Phys. Earth Planet. Inter. 107, 143–182.
O'Connor, J.M., Duncan, R.A., 1990. Evolution of the Walvis Ridge–Rio Grande Rise hot spot system: implications for African and South American plate motions over plumes. J. Geophys. Res. 95, 17475–17502.
O'Connor, J., Jokat, W., le Roex, A., Class, C., Wijbrans, J., Kessling, S., Kuiper, K., Nebel, O., 2012. Hotspot trails in the South Atlantic controlled by plume and plate tectonic processes. Nat. Geosci. 5, 735–738.
O'Mongain, A., Ottemoller, L., Brian, B., Galloway, D., Booth, D., 2007. Seismic activity associated with a probable submarine eruption near Tristan da Cunha, July 2004–July 2006. Seismol. Res. Lett. 78, 375–382.
Okrusch, M., Matthes, S., 2014. Mineralogie. Springer Spektrum http://dx.doi.org/10.1007/978-3-642-34660-6.
Putirka, K.D., 2008. Thermometers and barometers for volcanic systems. Rev. Mineral. Geochem. 69, 61–120.
Reagan, M.K., Turner, S., Legg, M., Sims, K.W.W., Hards, V.L., 2008. ^{238}U and ^{232}Th-decay series constraints on the timescales of crystal fractionation to produce the phonolite erupted in 2004 near Tristan da Cunha, South Atlantic Ocean. Geochim. Cosmochim. Acta 72, 4367–4378.
Rhodes, M., Dungan, M.A., Blanchard, D.P., Long, P.E., 1979. Magma mixing at mid-ocean ridges: evidence from basalts drilled 22° N on the mid-Atlantic ridge. Tectonophysics 55, 35–61.
Rocha-Junior, E.R.V., Marques, L.S., Babinski, M., Nardy, A.J.R., Figueiredo, A.M.G., Machado, F.B., 2013. Sr–Nd–Pb isotopic constraints on the nature of the mantle sources involved in the genesis of the high-Ti tholeiites from northern Paraná Continental Flood Basalts (Brazil). J. S. Am. Earth Sci. 46, 9–25.
Rocha-Junior, E.R.V., Puchtel, I.S., Marques, L.S., Walker, R.J., Machado, F.B., Nardy, A.J.R., Babinski, M., Figueiredo, A.M.G., 2012. Re–Os isotope and highly siderophile element systematics of the Paraná continental flood basalts (Brazil). Earth Planet. Sci. Lett. 337–338, 164–173 (1 July 2012).
Rohde, J.K., van den Bogaard, P., Hoernle, K., Hauff, F., Werner, R., 2012. Evidence for an age progression along the Tristan–Gough volcanic track from new ^{40}Ar/^{39}Ar ages on phenocryst phases. Tectonophysics 604, 60–71.
Rohde, J., Hoernle, K., Hauff, F., Werner, R., O'Connor, J., Class, C., Garbe-Schönberg, D., Jokat, W., 2013. 70 Ma chemical zonation of the Tristan–Gough hotspot track. Geology 41, 335–338.
Sack, R.O., Walker, D., Carmichael, I.S.E., 1987. Experimental petrology of alkalic lavas: constraints on cotectics of multiple saturation in natural basic liquids. Contrib. Mineral. Petrol. 96, 1–23.
Sobolev, A.V., 1996. Melt inclusions in minerals as a source of principle petrological information. Petrology 4, 209–222.
Stracke, A., Hofmann, A.W., Hart, S.R., 2005. FOZO, HIMU, and the rest of the mantle zoo. Geochem. Geophys. Geosyst. 6. http://dx.doi.org/10.1029/2004GC000824.
Stroncik, N.A., Hansteen, T.H., Kluegel, A., 2009. The magmatic plumbing system beneath El Hierro (Canary Islands): constraints from phenocrysts and naturally quenched basaltic glasses in submarine rocks. Contrib. Mineral. Petrol. 157, 593–607.
Thompson, R.N., Gibson, S.A., Dickin, A.P., Smith, P.M., 2001. Early Cretaceous basalt and picrite dykes of the southern Etendeka region, NW Namibia: windows into the role of the Tristan mantle plume in Parana–Etendeka magmatism. J. Petrol. 42, 2049–2081.
Trumbull, R.B., Bühn, B., Romer, R.L., Volker, F., 2003. The petrology of basanite–tephrite intrusions in the Erongo complex and implications for a plume source of Cretaceous alkaline complexes in Namibia. J. Petrol. 44, 93–112.

Please cite this article as: Weit, A., et al., The magmatic system beneath the Tristan da Cunha Island: Insights from thermobarometry, melting models and geophysics, Tectonophysics (2016), http://dx.doi.org/10.1016/j.tecto.2016.08.010